Title

Search for $B^- \to \Lambda_c + X \ell^- \bar{\nu}_\ell$ decays in events with a fully reconstructed B meson

Journal

Physical Review D, 85(1)

ISSN

2470-0010

Authors

Lees, JP
Poireau, V
Tisserand, V
et al.

Publication Date

2012

DOI

10.1103/physrevd.85.011102

B^0 meson decays to $\rho^0 K^{*0}$, $f_0 K^{*0}$, and $\rho^- K^{*+}$, including higher K^* resonances

J. P. Lees,[1] V. Poireau,[1] V. Tisserand,[1] J. Garra Tico,[2] E. Grauges,[2] M. Martinelli,[3a,3b] D. A. Milanes,[3a] A. Palano,[3a,3b] M. Pappagallo,[3a,3b] G. Eigen,[4] B. Stugu,[4] L. Sun,[4] D. N. Brown,[5] L. T. Kerth,[5] Yu. G. Kolomensky,[5] G. Lynch,[5] H. Koch,[6] T. Schroeder,[6] D. J. Asgeirsson,[7] C. Hearty,[7] T. S. Mattison,[7] J. A. McKenna,[7] A. Khan,[8] V. E. Blinov,[9] A. R. Buzykaev,[9] V. P. Druzhinin,[9] V. B. Golubev,[9] E. A. Kravchenko,[9] A. P. Onuchin,[9] S. I. Serednyakov,[9] Yu. I. Skovpen,[9] E. P. Solodov,[9] K. Yu. Todyshev,[9] A. N. Yushkov,[9] M. Bondioli,[10] D. Kirkby,[10] A. J. Lankford,[10] M. Mandelkern,[10] D. P. Stoker,[10] H. Atmacan,[11] J. W. Gary,[11] F. Liu,[11] O. Long,[11] G. M. Vitug,[11] C. Campagnari,[12] T. M. Hong,[12] D. Kovalskyi,[12] J. D. Richman,[12] C. A. West,[12] A. M. Eisner,[13] J. Kroseberg,[13] W. S. Lockman,[13] A. J. Martinez,[13] T. Schalk,[13] B. A. Schumm,[13] A. Seiden,[13] C. H. Cheng,[14] D. A. Doll,[14] B. Echenard,[14] K. T. Flood,[14] D. G. Hitlin,[14] P. Ongmongkolkul,[14] F. C. Porter,[14] A. Y. Rakitin,[14] R. Andreassen,[15] M. S. Dubrovin,[15] B. T. Meadows,[15] M. D. Sokoloff,[15] P. C. Bloom,[16] W. T. Ford,[16] A. Gaz,[16] M. Nagel,[16] U. Nauenberg,[16] J. G. Smith,[16] S. R. Wagner,[16] R. Ayad,[17,*] W. H. Toki,[17] B. Spaan,[18] M. J. Kobel,[19] K. R. Schubert,[19] R. Schwierz,[19] D. Bernard,[20] M. Verderi,[20] P. J. Clark,[21] S. Playfer,[21] D. Bettoni,[22a] C. Bozzi,[22a] R. Calabrese,[22a,22b] G. Cibinetto,[22a,22b] E. Fioravanti,[22a,22b] I. Garzia,[22a,22b] E. Luppi,[22a,22b] M. Munerato,[22a,22b] M. Negrini,[22a,22b] L. Piemontese,[22a] R. Baldini-Ferroli,[23] A. Calcaterra,[23] R. de Sangro,[23] G. Finocchiaro,[23] M. Nicolaci,[23] P. Patteri,[23] I. M. Peruzzi,[23,†] M. Piccolo,[23] M. Rama,[23] A. Zallo,[23] R. Contri,[24a,24b] E. Guido,[24a,24b] M. Lo Vetere,[24a,24b] M. R. Monge,[24a,24b] S. Passaggio,[24a] C. Patrignani,[24a,24b] E. Robutti,[24a] B. Bhuyan,[25] V. Prasad,[25] C. L. Lee,[26] M. Morii,[26] A. J. Edwards,[27] A. Adametz,[28] J. Marks,[28] U. Uwer,[28] F. U. Bernlochner,[29] M. Ebert,[29] H. M. Lacker,[29] T. Lueck,[29] P. D. Dauncey,[30] M. Tibbetts,[30] P. K. Behera,[31] U. Mallik,[31] C. Chen,[32] J. Cochran,[32] W. T. Meyer,[32] S. Prell,[32] E. I. Rosenberg,[32] A. E. Rubin,[32] A. V. Gritsan,[33] Z. J. Guo,[33] N. Arnaud,[34] M. Davier,[34] G. Grosdidier,[34] F. Le Diberder,[34] A. M. Lutz,[34] B. Malaescu,[34] P. Roudeau,[34] M. H. Schune,[34] A. Stocchi,[34] G. Wormser,[34] D. J. Lange,[35] D. M. Wright,[35] I. Bingham,[36] C. A. Chavez,[36] J. P. Coleman,[36] J. R. Fry,[36] E. Gabathuler,[36] D. E. Hutchcroft,[36] D. J. Payne,[36] C. Touramanis,[36] A. J. Bevan,[37] F. Di Lodovico,[37] R. Sacco,[37] M. Sigamani,[37] G. Cowan,[38] S. Paramesvaran,[38] D. N. Brown,[39] C. L. Davis,[39] A. G. Denig,[40] M. Fritsch,[40] W. Gradl,[40] A. Hafner,[40] E. Prencipe,[40] K. E. Alwyn,[41] D. Bailey,[41] R. J. Barlow,[41] G. Jackson,[41] G. D. Lafferty,[41] R. Cenci,[42] B. Hamilton,[42] A. Jawahery,[42] D. A. Roberts,[42] G. Simi,[42] C. Dallapiccola,[43] R. Cowan,[44] D. Dujmic,[44] G. Sciolla,[44] D. Lindemann,[45] P. M. Patel,[45] S. H. Robertson,[45] M. Schram,[45] P. Biassoni,[46a,46b] A. Lazzaro,[46a,46b] V. Lombardo,[46a] N. Neri,[46a,46b] F. Palombo,[46a,46b] S. Stracka,[46a,46b] L. Cremaldi,[47] R. Godang,[47,‡] R. Kroeger,[47] P. Sonnek,[47] D. J. Summers,[47] X. Nguyen,[48] P. Taras,[48] G. De Nardo,[49a,49b] D. Monorchio,[49a,49b] G. Onorato,[49a,49b] C. Sciacca,[49a,49b] G. Raven,[50] H. L. Snoek,[50] C. P. Jessop,[51] K. J. Knoepfel,[51] J. M. LoSecco,[51] W. F. Wang,[51] K. Honscheid,[52] R. Kass,[52] J. Brau,[53] R. Frey,[53] N. B. Sinev,[53] D. Strom,[53] E. Torrence,[53] E. Feltresi,[54a,54b] N. Gagliardi,[54a,54b] M. Margoni,[54a,54b] M. Morandin,[54a] M. Posocco,[54a] M. Rotondo,[54a] F. Simonetto,[54a,54b] R. Stroili,[54a,54b] E. Ben-Haim,[55] M. Bomben,[55] G. R. Bonneaud,[55] H. Briand,[55] G. Calderini,[55] J. Chauveau,[55] O. Hamon,[55] Ph. Leruste,[55] G. Marchiori,[55] J. Ocariz,[55] S. Sitt,[55] M. Biasini,[56a,56b] E. Manoni,[56a,56b] S. Pacetti,[56a,56b] A. Rossi,[56a,56b] C. Angelini,[57a,57b] G. Batignani,[57a,57b] S. Bettarini,[57a,57b] M. Carpinelli,[57a,57b,§] G. Casarosa,[57a,57b] A. Cervelli,[57a,57b] F. Forti,[57a,57b] M. A. Giorgi,[57a,57b] A. Lusiani,[57a,57c] B. Oberhof,[57a,57b] E. Paoloni,[57a,57b] A. Perez,[57a] G. Rizzo,[57a,57b] J. J. Walsh,[57a] D. Lopes Pegna,[58] C. Lu,[58] J. Olsen,[58] A. J. S. Smith,[58] A. V. Telnov,[58] F. Anulli,[59a] G. Cavoto,[59a] R. Faccini,[59a,59b] F. Ferrarotto,[59a] F. Ferroni,[59a,59b] M. Gaspero,[59a,59b] L. Li Gioi,[59a] M. A. Mazzoni,[59a] G. Piredda,[59a] C. Bünger,[60] O. Grünberg,[60] T. Hartmann,[60] T. Leddig,[60] H. Schröder,[60] R. Waldi,[60] T. Adye,[61] E. O. Olaiya,[61] F. F. Wilson,[61] S. Emery,[62] G. Hamel de Monchenault,[62] G. Vasseur,[62] Ch. Yèche,[62] D. Aston,[63] D. J. Bard,[63] R. Bartoldus,[63] C. Cartaro,[63] M. R. Convery,[63] J. Dorfan,[63] G. P. Dubois-Felsmann,[63] W. Dunwoodie,[63] R. C. Field,[63] M. Franco Sevilla,[63] B. G. Fulsom,[63] A. M. Gabareen,[63] M. T. Graham,[63] P. Grenier,[63] C. Hast,[63] W. R. Innes,[63] M. H. Kelsey,[63] H. Kim,[63] P. Kim,[63] M. L. Kocian,[63] D. W. G. S. Leith,[63] P. Lewis,[63] S. Li,[63] B. Lindquist,[63] S. Luitz,[63] V. Luth,[63] H. L. Lynch,[63] D. B. MacFarlane,[63] D. R. Muller,[63] H. Neal,[63] S. Nelson,[63] I. Ofte,[63] M. Perl,[63] T. Pulliam,[63] B. N. Ratcliff,[63] A. Roodman,[63] A. A. Salnikov,[63] V. Santoro,[63] R. H. Schindler,[63] A. Snyder,[63] D. Su,[63] M. K. Sullivan,[63] J. Va'vra,[63] A. P. Wagner,[63] M. Weaver,[63] W. J. Wisniewski,[63] M. Wittgen,[63] D. H. Wright,[63] H. W. Wulsin,[63] A. K. Yarritu,[63] C. C. Young,[63] V. Ziegler,[63] W. Park,[64] M. V. Purohit,[64] R. M. White,[64] J. R. Wilson,[64] A. Randle-Conde,[65] S. J. Sekula,[65] M. Bellis,[66] J. F. Benitez,[66] P. R. Burchat,[66] T. S. Miyashita,[66] M. S. Alam,[67] J. A. Ernst,[67] R. Gorodeisky,[68] N. Guttman,[68] D. R. Peimer,[68] A. Soffer,[68] P. Lund,[69] S. M. Spanier,[69] R. Eckmann,[70] J. L. Ritchie,[70] A. M. Ruland,[70] C. J. Schilling,[70] R. F. Schwitters,[70] B. C. Wray,[70] J. M. Izen,[71] X. C. Lou,[71] F. Bianchi,[72a,72b] D. Gamba,[72a,72b] L. Lanceri,[73a,73b] L. Vitale,[73a,73b] F. Martinez-Vidal,[74] A. Oyanguren,[74] H. Ahmed,[75] J. Albert,[75] Sw. Banerjee,[75] H. H. F. Choi,[75]

G. J. King,[75] R. Kowalewski,[75] M. J. Lewczuk,[75] C. Lindsay,[75] I. M. Nugent,[75] J. M. Roney,[75] R. J. Sobie,[75] T. J. Gershon,[76] P. F. Harrison,[76] T. E. Latham,[76] E. M. T. Puccio,[76] H. R. Band,[77] S. Dasu,[77] Y. Pan,[77] R. Prepost,[77] C. O. Vuosalo,[77] and S. L. Wu[77]

(*BABAR* Collaboration)

[1]*Laboratoire d'Annecy-le-Vieux de Physique des Particules (LAPP), Université de Savoie, CNRS/IN2P3, F-74941 Annecy-Le-Vieux, France*
[2]*Universitat de Barcelona, Facultat de Fisica, Departament ECM, E-08028 Barcelona, Spain*
[3a]*INFN Sezione di Bari, I-70126 Bari, Italy*
[3b]*Dipartimento di Fisica, Università di Bari, I-70126 Bari, Italy*
[4]*University of Bergen, Institute of Physics, N-5007 Bergen, Norway*
[5]*Lawrence Berkeley National Laboratory and University of California, Berkeley, California 94720, USA*
[6]*Ruhr Universität Bochum, Institut für Experimentalphysik 1, D-44780 Bochum, Germany*
[7]*University of British Columbia, Vancouver, British Columbia, Canada V6T 1Z1*
[8]*Brunel University, Uxbridge, Middlesex UB8 3PH, United Kingdom*
[9]*Budker Institute of Nuclear Physics, Novosibirsk 630090, Russia*
[10]*University of California at Irvine, Irvine, California 92697, USA*
[11]*University of California at Riverside, Riverside, California 92521, USA*
[12]*University of California at Santa Barbara, Santa Barbara, California 93106, USA*
[13]*University of California at Santa Cruz, Institute for Particle Physics, Santa Cruz, California 95064, USA*
[14]*California Institute of Technology, Pasadena, California 91125, USA*
[15]*University of Cincinnati, Cincinnati, Ohio 45221, USA*
[16]*University of Colorado, Boulder, Colorado 80309, USA*
[17]*Colorado State University, Fort Collins, Colorado 80523, USA*
[18]*Technische Universität Dortmund, Fakultät Physik, D-44221 Dortmund, Germany*
[19]*Technische Universität Dresden, Institut für Kern- und Teilchenphysik, D-01062 Dresden, Germany*
[20]*Laboratoire Leprince-Ringuet, Ecole Polytechnique, CNRS/IN2P3, F-91128 Palaiseau, France*
[21]*University of Edinburgh, Edinburgh EH9 3JZ, United Kingdom*
[22a]*INFN Sezione di Ferrara, I-44100 Ferrara, Italy*
[22b]*Dipartimento di Fisica, Università di Ferrara, I-44100 Ferrara, Italy*
[23]*INFN Laboratori Nazionali di Frascati, I-00044 Frascati, Italy*
[24a]*INFN Sezione di Genova, I-16146 Genova, Italy*
[24b]*Dipartimento di Fisica, Università di Genova, I-16146 Genova, Italy*
[25]*Indian Institute of Technology Guwahati, Guwahati, Assam, 781 039, India*
[26]*Harvard University, Cambridge, Massachusetts 02138, USA*
[27]*Harvey Mudd College, Claremont, California 91711*
[28]*Universität Heidelberg, Physikalisches Institut, Philosophenweg 12, D-69120 Heidelberg, Germany*
[29]*Humboldt-Universität zu Berlin, Institut für Physik, Newtonstr. 15, D-12489 Berlin, Germany*
[30]*Imperial College London, London, SW7 2AZ, United Kingdom*
[31]*University of Iowa, Iowa City, Iowa 52242, USA*
[32]*Iowa State University, Ames, Iowa 50011-3160, USA*
[33]*Johns Hopkins University, Baltimore, Maryland 21218, USA*
[34]*Laboratoire de l'Accélérateur Linéaire, IN2P3/CNRS et Université Paris-Sud 11, Centre Scientifique d'Orsay, B. P. 34, F-91898 Orsay Cedex, France*
[35]*Lawrence Livermore National Laboratory, Livermore, California 94550, USA*
[36]*University of Liverpool, Liverpool L69 7ZE, United Kingdom*
[37]*Queen Mary, University of London, London, E1 4NS, United Kingdom*
[38]*University of London, Royal Holloway and Bedford New College, Egham, Surrey TW20 0EX, United Kingdom*
[39]*University of Louisville, Louisville, Kentucky 40292, USA*
[40]*Johannes Gutenberg-Universität Mainz, Institut für Kernphysik, D-55099 Mainz, Germany*
[41]*University of Manchester, Manchester M13 9PL, United Kingdom*
[42]*University of Maryland, College Park, Maryland 20742, USA*
[43]*University of Massachusetts, Amherst, Massachusetts 01003, USA*
[44]*Massachusetts Institute of Technology, Laboratory for Nuclear Science, Cambridge, Massachusetts 02139, USA*
[45]*McGill University, Montréal, Québec, Canada H3A 2T8*
[46a]*INFN Sezione di Milano, I-20133 Milano, Italy*
[46b]*Dipartimento di Fisica, Università di Milano, I-20133 Milano, Italy*
[47]*University of Mississippi, University, Mississippi 38677, USA*

[48]*Université de Montréal, Physique des Particules, Montréal, Québec, Canada H3C 3J7*
[49a]*INFN Sezione di Napoli, I-80126 Napoli, Italy*
[49b]*Dipartimento di Scienze Fisiche, Università di Napoli Federico II, I-80126 Napoli, Italy*
[50]*NIKHEF, National Institute for Nuclear Physics and High Energy Physics, NL-1009 DB Amsterdam, The Netherlands*
[51]*University of Notre Dame, Notre Dame, Indiana 46556, USA*
[52]*Ohio State University, Columbus, Ohio 43210, USA*
[53]*University of Oregon, Eugene, Oregon 97403, USA*
[54a]*INFN Sezione di Padova, I-35131 Padova, Italy*
[54b]*Dipartimento di Fisica, Università di Padova, I-35131 Padova, Italy*
[55]*Laboratoire de Physique Nucléaire et de Hautes Energies, IN2P3/CNRS, Université Pierre et Marie Curie-Paris6, Université Denis Diderot-Paris7, F-75252 Paris, France*
[56a]*INFN Sezione di Perugia, I-06100 Perugia, Italy*
[56b]*Dipartimento di Fisica, Università di Perugia, I-06100 Perugia, Italy*
[57a]*INFN Sezione di Pisa, I-56127 Pisa, Italy*
[57b]*Dipartimento di Fisica, Università di Pisa, I-56127 Pisa, Italy*
[57c]*Scuola Normale Superiore di Pisa, I-56127 Pisa, Italy*
[58]*Princeton University, Princeton, New Jersey 08544, USA*
[59a]*INFN Sezione di Roma, I-00185 Roma, Italy*
[59b]*Dipartimento di Fisica, Università di Roma La Sapienza, I-00185 Roma, Italy*
[60]*Universität Rostock, D-18051 Rostock, Germany*
[61]*Rutherford Appleton Laboratory, Chilton, Didcot, Oxon, OX11 0QX, United Kingdom*
[62]*CEA, Irfu, SPP, Centre de Saclay, F-91191 Gif-sur-Yvette, France*
[63]*SLAC National Accelerator Laboratory, Stanford, California 94309 USA*
[64]*University of South Carolina, Columbia, South Carolina 29208, USA*
[65]*Southern Methodist University, Dallas, Texas 75275, USA*
[66]*Stanford University, Stanford, California 94305-4060, USA*
[67]*State University of New York, Albany, New York 12222, USA*
[68]*Tel Aviv University, School of Physics and Astronomy, Tel Aviv, 69978, Israel*
[69]*University of Tennessee, Knoxville, Tennessee 37996, USA*
[70]*University of Texas at Austin, Austin, Texas 78712, USA*
[71]*University of Texas at Dallas, Richardson, Texas 75083, USA*
[72a]*INFN Sezione di Torino, I-10125 Torino, Italy*
[72b]*Dipartimento di Fisica Sperimentale, Università di Torino, I-10125 Torino, Italy*
[73a]*INFN Sezione di Trieste, I-34127 Trieste, Italy*
[73b]*Dipartimento di Fisica, Università di Trieste, I-34127 Trieste, Italy*
[74]*IFIC, Universitat de Valencia-CSIC, E-46071 Valencia, Spain*
[75]*University of Victoria, Victoria, British Columbia, Canada V8W 3P6*
[76]*Department of Physics, University of Warwick, Coventry CV4 7AL, United Kingdom*
[77]*University of Wisconsin, Madison, Wisconsin 53706, USA*
(Received 19 December 2011; published 27 April 2012)

We present branching fraction measurements for the decays $B^0 \to \rho^0 K^{*0}$, $B^0 \to f_0 K^{*0}$, and $B^0 \to \rho^- K^{*+}$, where K^* is an S-wave $(K\pi)_0^*$ or a $K^*(892)$ meson; we also measure $B^0 \to f_0 K_2^*(1430)^0$. For the $K^*(892)$ channels, we report measurements of longitudinal polarization fractions (for ρ final states) and direct CP violation asymmetries. These results are obtained from a sample of $(471.0 \pm 2.8) \times 10^6$ $B\overline{B}$ pairs collected with the *BABAR* detector at the PEP-II asymmetric-energy e^+e^- collider at the SLAC National Accelerator Laboratory. We observe $\rho^0 K^*(892)^0$, $\rho^0(K\pi)_0^{*0}$, $f_0 K^*(892)^0$, and $\rho^- K^*(892)^+$ with greater than 5σ significance, including systematics. We report first evidence for $f_0(K\pi)_0^{*0}$ and $f_0 K_2^*(1430)^0$, and place an upper limit on $\rho^-(K\pi)_0^{*+}$. Our results in the $K^*(892)$ channels are consistent with no direct CP violation.

DOI: 10.1103/PhysRevD.85.072005 PACS numbers: 13.25.Hw, 11.30.Er, 12.15.Hh

I. INTRODUCTION

Measurements of the branching fractions and angular distributions of B meson decays to hadronic final states without a charm quark probe the dynamics of both the weak and strong interactions. Such studies also play an important role in understanding CP violation in the quark

*Now at Temple University, Philadelphia, PA 19122, USA
†Also with Università di Perugia, Dipartimento di Fisica, Perugia, Italy
‡Now at University of South Alabama, Mobile, AL 36688, USA
§Also with Università di Sassari, Sassari, Italy

sector and in searching for evidence for physics beyond the Standard Model [1].

We report measurements of branching fractions for the decays $B^0 \to \rho^0 K^*(892)^0$, $B^0 \to f_0 K^*(892)^0$, $B^0 \to \rho^- K^*(892)^+$, $B^0 \to \rho^0 (K\pi)_0^{*0}$, $B^0 \to f_0 (K\pi)_0^{*0}$, $B^0 \to \rho^- (K\pi)_0^{*+}$, and $B^0 \to f_0 K_2^*(1430)^0$. For the $\rho K^*(892)$ channels, we measure the longitudinal fraction f_L, and for all $K^*(892)$ channels we measure charge asymmetries $\mathcal{A}_{\rm ch}$. The notation ρ refers to the $\rho(770)$ [2] and f_0 to the $f_0(980)$ [3]. Throughout this paper, we use K^* to refer to any of the scalar $(K\pi)_0^*$, vector $K^*(892)$, or tensor $K_2^*(1430)$ states [2]. The notation $(K\pi)_0^*$ refers to the scalar $K\pi$, which we describe with a LASS model [4,5], combining the $K_0^*(1430)$ resonance with an effective-range nonresonant component. Charge-conjugate modes are implied throughout this paper.

The charmless decays $B \to \rho K^*$ proceed through dominant penguin loops and Cabibbo-Kobayashi-Maskawa–suppressed tree processes ($B^+ \to \rho^+ K^{*0}$ is pure penguin), as shown in Fig. 1. Naïve factorization models predict a large longitudinal polarization fraction f_L (of order $(1 - 4m_V^2/m_B^2) \sim 0.9$) for vector-vector ($VV$) decays, where m_V and m_B are the masses of the vector and B mesons, respectively [1]. However, measurements of penguin-dominated VV decays, such as the previous measurements of $B^0 \to \rho^0 K^*(892)^0$ and $B^+ \to \rho^+ K^*(892)^0$ [6,7], find $f_L \sim 0.5$; a recent *BABAR* measurement of $B^+ \to \rho^0 K^*(892)^+$ finds $f_L = 0.78 \pm 0.12$ [8]. Recent predictions in QCD factorization (QCDF) [9] can accommodate $f_L \sim 0.5$, although correctly predicting both the branching fraction and f_L remains a challenge.

Both the *BABAR* and Belle Collaborations have previously measured the branching fractions of $B^0 \to \rho^0 K^*(892)^0$ and $B^0 \to f_0 K^*(892)^0$. *BABAR* has also placed a 90% confidence level (C.L.) upper limit on $B^0 \to \rho^- K^*(892)^+$ [6,7]. Belle searched for nonresonant $B^0 \to \rho^0 K^+ \pi^-$ and $f_0 K^+ \pi^-$ decays, finding a 5 standard deviation (5σ) significant result for $\rho^0 K^+ \pi^-$ [7]. Decays involving a ρ or f_0 along with a $(K\pi)_0^*$ or $K_2^*(1430)$ have not been the subject of previous studies. Predictions exist from both QCDF [9] and perturbative QCD (pQCD) [10] for the branching fractions ($\mathcal{B}$) of the $\rho K_0^*(1430)$ channels, with QCDF predicting values $\mathcal{O}(\text{few} \times 10^{-5})$ and pQCD $\mathcal{O}(5 \times 10^{-7} - 10^{-5})$. Improved experimental measurements will help refine predictions and constrain physics beyond the Standard Model.

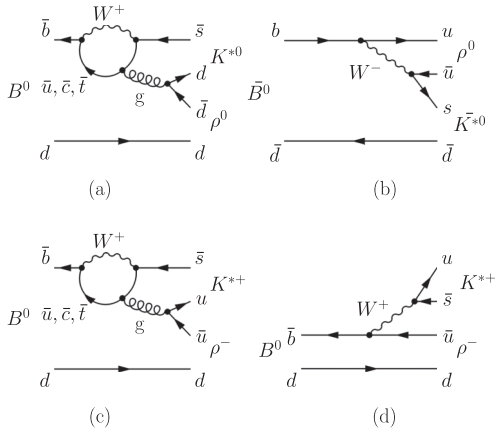

FIG. 1. Feynman diagrams for (a–b) $B^0 \to \rho^0 K^{*0}$ and (c–d) $B^0 \to \rho^- K^{*+}$. Gluonic penguin diagrams (a, c) dominate over tree (b, d) contributions.

The decays $B^0 \to \rho^0 K^*(892)^0$ and $B^0 \to \rho^- K^*(892)^+$ are of the form $B \to VV$; these decays have 3 polarization states, which are, in principle, accessible experimentally. In practice, a full angular analysis requires a large number of signal events. In the analyses described in this paper, we integrate over the azimuthal angle (the angle between the two vector meson decay planes). The azimuthal angle is not correlated with any specific direction in the detector, so we assume a uniform acceptance over this angle. We define the helicity angles θ_{K^*} and θ_ρ and the azimuthal angle ϕ, as shown in Fig. 2. The helicity angles are defined in the rest frame of the vector meson: θ_{K^*} is the angle between the charged kaon and the B meson in the K^* rest frame; θ_ρ is the angle between the positively charged (or only charged) pion and the B meson in the ρ rest frame. In the analysis of the $K^*(892)$ channels, we make use of the helicity observables, defined for $\alpha = \rho, K^*$ as $\mathcal{H}_\alpha = \cos(\theta_\alpha)$. Occasionally, we refer to a specific charge state, e.g. ρ^0, which we indicate with the notation $\mathcal{H}_{\rho^0} = \cos(\theta_{\rho^0})$.

The longitudinal polarization fraction f_L for $B^0 \to \rho K^*(892)$ can be extracted from the differential decay rate, parameterized as a function of θ_{K^*} and θ_ρ:

$$\frac{1}{\Gamma}\frac{d^2\Gamma}{d\cos\theta_{K^*} d\cos\theta_\rho} \propto \frac{1}{4}(1 - f_L)\sin^2\theta_{K^*}\sin^2\theta_\rho + f_L\cos^2\theta_{K^*}\cos^2\theta_\rho. \quad (1)$$

The CP-violating asymmetry is defined as

$$\mathcal{A}_{\rm ch} \equiv \frac{\Gamma^- - \Gamma^+}{\Gamma^- + \Gamma^+}, \quad (2)$$

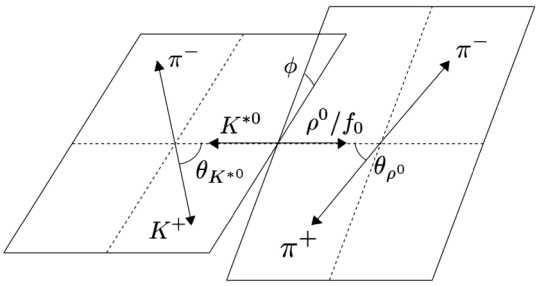

FIG. 2. Definition of the helicity angles for $B^0 \to \rho^0 K^{*0}$.

where the superscript on the decay width Γ refers to the charge of the kaon from the K^* decay.

All results in this paper are based on extended maximum likelihood (ML) fits as described in Sec. VI. In each analysis, loose criteria are used to select events likely to contain the desired signal B decay (Sec. III, IV, and V). A fit to kinematic and topological discriminating variables is used to differentiate between signal and background events and to determine signal event yields, CP-violating asymmetries, and longitudinal polarization fractions, where appropriate. In all of the decays analyzed, the background is dominated by random particle combinations in continuum ($e^+e^- \to q\bar{q}$, $q = u, d, s, c$) events. Although $q\bar{q}$ background dominates the selected data sample, background from other $B\bar{B}$ decays tends to have more signal-like distributions in the discriminating variables. The dominant $B\bar{B}$ backgrounds are accounted for separately in the ML fit, as discussed in Sec. IV D. Signal event yields are converted into branching fractions via selection efficiencies determined from Monte Carlo (MC) simulations of the signal as well as auxiliary studies of the data.

II. DETECTOR AND DATA

For this analysis, we use the full *BABAR* data set, collected at the PEP-II asymmetric-energy e^+e^- collider located at the SLAC National Accelerator Laboratory. The data set consists of $(471.0 \pm 2.8) \times 10^6$ $B\bar{B}$ pairs originating from the decay of the $\Upsilon(4S)$ resonance, produced at a center-of-mass (CM) energy $\sqrt{s} = 10.58$ GeV. This effectively doubles the data set from the previous *BABAR* measurement [6].

The asymmetric beam configuration in the laboratory frame provides a boost to the $\Upsilon(4S)$ of $\beta\gamma = 0.56$. This results in a charged particle laboratory momentum spectrum from B decays with an end point near 4 GeV. Charged particles are detected and their momenta measured by the combination of a silicon vertex tracker, consisting of 5 layers of double-sided detectors and a 40-layer central drift chamber, both operating in the 1.5-T magnetic field of a solenoid. For charged particles within the detector acceptance, the average detection efficiency is in excess of 96% per particle.

Photons are detected and their energies measured by a CsI(Tl) electromagnetic calorimeter (EMC). The measured π^0 mass resolution for π^0s with laboratory momentum in excess of 1 GeV is approximately 8 MeV.

Charged particle identification (PID) is provided by the average energy loss in the tracking devices and by an internally reflecting ring-imaging Cherenkov detector covering the central region. Additional information that we use to identify and reject electrons and muons is provided by the EMC and the detectors installed in a segmented solenoid flux return. The *BABAR* detector is described in detail in Ref. [11].

III. CANDIDATE RECONSTRUCTION AND B MESON SELECTION

We reconstruct B daughter candidates through their decays $\rho^0 \to \pi^+\pi^-$, $f_0 \to \pi^+\pi^-$, $\rho^- \to \pi^-\pi^0$, $K^{*0} \to K^+\pi^-$, $K^{*+} \to K^+\pi^0$, and $\pi^0 \to \gamma\gamma$. We apply the same selection criteria for f_0 and ρ^0 candidates.

The $K^*(892)$ channels are analyzed separately from the $(K\pi)_0^*$ and $K_2^*(1430)$ decays, although the analyses share many similarities, including most event selection requirements. Where the analyses differ, we specify the $K^*(892)$ channels as the "low mass region" (LMR), distinguished by the $K\pi$ mass requirement of $750 < m_{K\pi} < 1000$ MeV. The $(K\pi)_0^*$ and $K_2^*(1430)$ analyses are performed in the "high mass region" (HMR), $1000 < m_{K\pi} < 1550$ MeV.

The invariant masses of the B daughter candidates must satisfy the following requirements: $120 < m_{\gamma\gamma} < 150$ MeV, and either $470 < m_{\pi\pi} < 1070$ MeV (LMR) or $470 < m_{\pi\pi} < 1200$ MeV (HMR). The $\pi\pi$ and $K\pi$ mass intervals are chosen to include sidebands large enough to parameterize the backgrounds.

All photons are required to appear as a single cluster of energy in the EMC, not matched with any track, and to have a maximum lateral moment of 0.8. We require the energy of the photons to be greater than 50 MeV and the π^0 energy to be greater than 250 MeV, both in the laboratory frame. All charged tracks are required to originate from within 10 cm of the beamspot in the direction along the beam axis and within 1.5 cm in the plane perpendicular to that axis. Charged kaon candidates are additionally required to have at least 12 hits in the drift chamber and a transverse momentum of $p_T > 100$ MeV. The charged tracks are identified either as pions or kaons by measuring the energy loss in the tracking devices, the number of photons recorded by the ring-imaging Cherenkov detector, and the corresponding Cherenkov angle; these measurements are combined with information from the EMC and the flux return, where appropriate, to reject electrons, muons, and protons.

When reconstructing ρ^- and K^{*+} candidates, the mass of the π^0 candidate is constrained to its nominal value [2]. The π^0 is constrained to originate from the interaction point, taking into account the finite B meson flight distance; the charged track is required to originate from the interaction point. For ρ^0 and K^{*0} candidates, the 2 charged tracks are required to originate from a common vertex, as determined by a generalized least squares minimization using Lagrange multipliers; we require the change in χ^2 between two successive iterations in the fitter to be less than 0.005, with a maximum of 6 iterations. The B meson candidate is formed by performing a global Kalman fit to the entire decay chain.

A B meson candidate is characterized kinematically by the energy-substituted mass $m_{\rm ES}$ and the energy difference ΔE, defined in the $\Upsilon(4S)$ frame as

$$m_{\rm ES} = \sqrt{\frac{1}{4}s - \mathbf{p}_B^{*2}} \quad \text{and} \quad \Delta E = E_B^* - \frac{1}{2}\sqrt{s},$$

where $q_B^* = (E_B^*, \mathbf{p}_B^*)$ is the four momentum of the B candidate in the $\Upsilon(4S)$ frame and s is the square of the invariant mass of the electron-positron system. $m_{\rm ES}$ and ΔE are favorable observables because they are nearly uncorrelated. The small correlation is accounted for in the correction of the fit bias (see Sec. IX). Correctly reconstructed signal events peak at zero in ΔE and at the B mass [2] in $m_{\rm ES}$, with a resolution in $m_{\rm ES}$ of around 2.5 MeV and in ΔE of 17–37 MeV. We select events with $5.26 < m_{\rm ES} < 5.2893$ GeV. For $\rho^0 K^{*0}$, we require $|\Delta E| < 0.10$ GeV, while for $\rho^- K^{*+}$, we allow $-0.17 < \Delta E < 0.10$ GeV to account for a long low-side tail resulting from poorly reconstructed π^0s.

IV. SOURCES OF BACKGROUND AND SUPPRESSION TECHNIQUES

Production of $B\bar{B}$ pairs accounts for only about 25% of the total hadronic cross-section at the $\Upsilon(4S)$ peak. The bulk of the cross-section arises from continuum events. Tau-pair production and other QED processes contribute as well. We describe in the following the main sources of background and discuss techniques for distinguishing them from signal.

A. QED and tau-pair backgrounds

Two-photon processes, Bhabha scattering, muon- and tau-pair production are characterized by low charged track multiplicities. Bhabha and muon-pair events are significantly prescaled at the trigger level. We further suppress these and other tau and QED processes via a minimum requirement on the event track multiplicity. We require the event to contain at least 1 track more than the topology of our final state. These selection criteria are more than 90% efficient when applied to signal. From MC simulations [12], we determine that the remaining background from these sources is negligible.

B. QCD continuum backgrounds

The dominant background arises from random combinations of particles in continuum $e^+e^- \to q\bar{q}$ events ($q = u, d, s, c$). The angle θ_T between the thrust axis [13] of the B candidate in the $\Upsilon(4S)$ rest frame and that of the remaining particles in the event is used to suppress this background. Jetlike continuum events peak at values of $|\cos\theta_{\rm T}|$ close to 1, while spherical B decays exhibit a flat distribution for this variable. We require that events satisfy $|\cos\theta_{\rm T}| < 0.7$.

Further rejection is achieved by restricting the range of the helicity angle $\mathcal{H}$ of the ρ and K^* mesons (see Fig. 2). We require $|\mathcal{H}_{\rho^0}| < 0.9$, $-0.8 < \mathcal{H}_{\rho^+} < 0.9$, $-0.85 < \mathcal{H}_{K^{*0}} < 1.0$, and $-0.8 < \mathcal{H}_{K^{*+}} < 1.0$. These requirements reject regions of phase space with low momentum π^+s and π^0s, where backgrounds are typically large.

Additional separation of signal and background is provided by a Fisher discriminant $\mathcal{F}$ exploiting 4 variables sensitive to the production dynamics and event shape: the polar angles (with respect to the beam axis in the e^+e^- CM frame) of the B candidate momentum and of the B thrust axis; and the zeroth and second angular moments $L_{0,2}$ of the energy flow, excluding the B candidate. The moments are defined in the CM frame by

$$L_j = \sum_i p_i |\cos\theta_i|^j, \tag{3}$$

where i labels a track or EMC cluster, θ_i is its angle with respect to the B thrust axis, and p_i is its momentum.

We find that $\mathcal{F}$ in continuum background is mildly correlated with the tagging category [14], which identifies the flavor of the other B in the event and places it into one of 6 categories based upon how it is identified. Although the tagging category is not used elsewhere in this analysis, we find that the overall signal-to-background separation provided by $\mathcal{F}$ can be slightly improved by removing this correlation. For each tagging category as well as for the category for which no B tag is assigned, we fit the $\mathcal{F}$ distribution with a Gaussian with different widths above and below the mean. We then shift the mean of the $\mathcal{F}$ distribution in each tagging category to align it with the average value of the $\mathcal{F}$ means in all tagging categories. The $\mathcal{F}$ distributions typically have a mean around -0.25 with an average width around 0.45; shifts are less than 0.03 for all categories except for the lepton-tagged events (the tagging category with the highest purity), for which the shift is about 0.35. The Fisher variable provides about 1 standard deviation of discrimination between B decay events and continuum background.

C. $B \to$ charm backgrounds

We suppress the background from B mesons decaying to charm by forming the invariant mass m_D from combinations of 2 or 3 out of the four daughter particles' four-momenta. For $\rho^0 K^{*0}$, we consider D candidates decaying to $K^-\pi^+$ and $K^-\pi^+\pi^+$. For $\rho^- K^{*+}$, we consider the combinations $K^-\pi^+$ and $K^-\pi^+\pi^0$. The event is retained only if $|m_D - m_D^{\rm PDG}| > 40$ MeV for all cases, except for the D meson formed with $K^+\pi^-$ in the $\rho^- K^{*+}$ channel, where we require $|m_D - m_D^{\rm PDG}| > 20$ MeV; $m_D^{\rm PDG}$ is the nominal D^+ or D^0 meson mass [2].

These D vetoes greatly reduce the amount of $B \to$ charm background in our samples, but as many of these channels have large branching fractions $\mathcal{O}(10^{-1} - 10^{-3})$, we include several charm backgrounds as separate components of the maximum likelihood fit, as detailed in Sec. IV D.

TABLE I. $B\bar{B}$ background categories for $B^0 \to \rho^0 K^{*0}$ and expected yields in the LMR and HMR.

$\rho^0 K^{*0}$ background	LMR	HMR
$B^0 \to \rho^0 (K\pi)_0^{*0}$	215 ± 34	...
$B^0 \to f_0 (K\pi)_0^{*0}$	19 ± 6	...
$B^0 \to f_2(1270) K^*(892)^0$	47 ± 3	...
$B^0 \to a_1^- K^+$	15 ± 3	40 ± 9
$B^0 \to D^- \pi^+$	209 ± 10	922 ± 45
$B \to \bar{D}^0 X$	433 ± 23	1798 ± 83
charmless cocktail	76 ± 22	149 ± 34

D. $B\bar{B}$ backgrounds

Although the dominant background arises from continuum $q\bar{q}$ events, care must be taken to describe the backgrounds from other B decays, as they have more signal-like distributions in many observables. For $\rho^0 K^*(892)^0$, we consider seven $B\bar{B}$ background categories: $B^0 \to \rho^0 (K\pi)_0^{*0}$; $B^0 \to f_0 (K\pi)_0^{*0}$; $B^0 \to f_2(1270) K^*(892)^0$ with $f_2(1270) \to \pi^+\pi^-$; $B^0 \to a_1^- K^+$ with $a_1^- \to \rho^0 \pi^-$; $B^0 \to D^- \pi^+$ with $D^- \to K^+ \pi^- \pi^-$; a combination of three $B \to \bar{D}^0 X$ channels with $\bar{D}^0 \to K^+ \pi^- \pi^0$; and a branching fraction-weighted combination of 13 other dominant charmless B decay channels (charmless cocktail), which have a high probability of passing our selection. The dominant channels in the charmless cocktail are $B^+ \to a_1^0 K^+$ with $a_1^0 \to \rho^- \pi^+$ and $B^+ \to \eta' K^+$ with $\eta' \to \rho^0 \gamma$. Most channels in the cocktail include a real ρ^0 or K^{*0}. The number of expected events in each category is given in Table I.

For the $(K\pi)_0^{*0}$ and $f_0 K_2^*(1430)^0$ signals, the background categories are the same, except that the $K^*(892)^0$ replaces the $(K\pi)_0^{*0}$ in the first two background categories. As will be described in Sec. VI B, the first stage of the fit to the HMR is insensitive to the composition of the $\pi^+\pi^-$ mass spectrum; therefore $\rho^0 K^*(892)^0$, $f_0 K^*(892)^0$, and $f_2(1270) K^*(892)^0$ are included in the same $K^*(892)^0$ category. Additionally, due to the wider $K^+\pi^-$ mass range in the HMR, 28 charmless B decay channels are combined in the charmless cocktail.

In analyzing $\rho^- K^*(892)^+$, we consider four $B\bar{B}$ background categories: $B^0 \to \rho^- (K\pi)_0^{*+}$, $B^0 \to a_1^- K^+$ with $a_1^- \to \rho^- \pi^0$, $B^0 \to \rho^+ \rho^-$, and $B^- \to \bar{D}^0 \rho^-$ with $\bar{D}^0 \to K^+ \pi^- \pi^0$. The number of expected events in each category is given in Table II. For the HMR, $\rho^- K^*(892)^+$ replaces the signal mode $\rho^- (K\pi)_0^{*+}$ as a background; the other categories remain the same.

TABLE II. $B\bar{B}$ background categories for $B^0 \to \rho^- K^{*+}$ and expected yields in the LMR and HMR.

$\rho^- K^{*+}$ background	LMR	HMR
$B^0 \to \rho^- (K\pi)_0^{*+}$	60 ± 23	...
$B^0 \to a_1^- K^+$	7 ± 2	13 ± 3
$B^0 \to \rho^+ \rho^-$	9 ± 1	15 ± 2
$B^- \to \bar{D}^0 \rho^-$	129 ± 17	427 ± 58

In the HMR fits, the $K^*(892)$ yields are allowed to float. The HMR $(K\pi)_0^*$ yields are extrapolated into the LMR using a ratio of LMR to HMR MC efficiencies; these $(K\pi)_0^*$ background yields are then fixed in the LMR fits. The $B^0 \to f_2(1270) K^*(892)^0$ background yield is determined using a high $m_{\pi^+\pi^-}$ sideband, as described in Sec. VIII; this yield is fixed in the $\rho^0 K^*(892)^0$ fit.

All other $B\bar{B}$ backgrounds are modeled from the simulation, with yields fixed to experimentally measured branching fraction $\mathcal{B}$ values [2]. For a few channels entering the charmless cocktail, no $\mathcal{B}$ measurements exist; in those cases, theory predictions are combined with other estimates and a 100% uncertainty is assigned to the branching fractions. These unmeasured charmless channels account for approximately 26% of the charmless cocktail background in the LMR and 40% in the HMR (see Table I). Uncertainties on the $B\bar{B}$ branching fractions are accounted for as systematic uncertainties (see Sec. XI).

V. FINAL SAMPLE CRITERIA

After all selection criteria discussed in Sec. III and IV have been applied, the average number of combinations per event in data is 1.02 for $\rho^0/f_0 K^{*0}$ and 1.16 for $\rho^- K^{*+}$. We select the candidate with the highest χ^2 probability in a geometric fit to a common B decay vertex. In this way, the probability of selecting the correctly reconstructed event is a few percent higher with respect to a random selection.

The sample sizes for the decay chains reported here range from 9,700 to 37,000 events, where we include sidebands in all discriminating variables (except the helicities) in order to parameterize the backgrounds.

VI. MAXIMUM LIKELIHOOD FIT

The candidates that satisfy the selection criteria described in Secs. III, IV, and V are subjected to an unbinned, extended maximum likelihood fit to extract signal yields. In all fits, the signal and $B\bar{B}$ background components are modeled with a Monte Carlo simulation of the decay process that includes the response of the detector and reconstruction chain [12].

A. Low mass region fit

In the low mass region, we obtain the yields, charge asymmetries $\mathcal{A}_{\rm ch}$, and longitudinal polarization fractions f_L from extended maximum likelihood fits to the seven observables: ΔE, $m_{\rm ES}$, $\mathcal{F}$, and the masses and helicities of the two resonance candidates ($m_{\pi\pi}$, $m_{K\pi}$, $\mathcal{H}_\rho$, and $\mathcal{H}_{K^*}$). The fits distinguish among several categories: $q\bar{q}$ background, $B\bar{B}$ background (see Sec. IV D), and signal. The signals $\rho^0 K^*(892)^0$ and $f_0 K^*(892)^0$ are fit simultaneously. For each event i and category j, we define the probability density functions (PDFs) $\mathcal{P}_j^i$ as

$$\mathcal{P}_j^i = \mathcal{P}_j(m_{\rm ES}{}^i)\mathcal{P}_j(\Delta E^i)\mathcal{P}_j(\mathcal{F}^i)\mathcal{P}_j(m^i_{\pi\pi})\mathcal{P}_j(m^i_{K\pi}) \times \mathcal{P}_j(\mathcal{H}^i_\rho)\mathcal{P}_j(\mathcal{H}^i_{K^*}), \quad (4)$$

with the resulting likelihood $\mathcal{L}$:

$$\mathcal{L} = \frac{e^{-\Sigma_j Y_j}}{N!}\prod_{i=1}^{N}\sum_j Y_j \mathcal{P}^i_j, \quad (5)$$

where Y_j is the fitted yield for category j and N is the number of events entering the fit. For the ρ^0/f_0 analysis, we use the absolute value of $\mathcal{H}_\rho$ in the fit, as the distribution is symmetric. We split the yields by the flavor of the decaying B meson in order to measure $\mathcal{A}_{\rm ch}$. We find correlations among the observables to be occasionally as high as 30% in simulations of the $B\bar{B}$ backgrounds, whereas they are small in the data samples, which are dominated by $q\bar{q}$ background. In signal, correlations are typically less than 1% and occasionally as large as 14%. Correlations among observables are accounted for by evaluating the fit bias (see Sec. IX).

B. High mass region fit

In the high mass region, the ML fit uses the five observables: ΔE, $m_{\rm ES}$, $\mathcal{F}$, $m_{\pi\pi}$, and $m_{K\pi}$. For $\rho^-(K\pi)_0^{*+}$, these five observables are combined in an extended ML fit, as previously cited.

For the $\rho^0/f_0(K\pi)_0^{*0}$ and $f_0K_2^*(1430)^0$ channels, we perform the ML fit in two stages. Because of the potential complexity of the resonant and nonresonant structures in the $\pi^+\pi^-$ and $K^+\pi^-$ invariant mass spectra, as well as the fact that many of these structures are quite broad, nontrivial correlations exist between several of the ML fit hypotheses. Attempts to perform the fit in a single stage using simulated data (see Sec. IX for the general procedure) demonstrate unacceptable convergence rates in some scenarios. Removing $m_{\pi\pi}$ from the ML fit greatly improves the convergence rates. We therefore employ a two-stage procedure for these HMR fits. In the first step, we perform an ML fit using only ΔE, $m_{\rm ES}$, $\mathcal{F}$, and $m_{K\pi}$; this allows us to separate out "inclusive" $(K\pi)_0^{*0}$ and $K_2^*(1430)^0$ signal from $q\bar{q}$ and $B\bar{B}$ backgrounds. If we observe sufficient (greater than 3σ statistical significance) signal in the inclusive K^{*0} channels, we perform a second-stage ML fit to $m_{\pi\pi}$ for selected signal events. Technical details are given below.

The PDF for the first-stage fit can be written as

$$\mathcal{P}^{\,i}_j = \mathcal{P}_j(m_{\rm ES}{}^i)\mathcal{P}_j(\Delta E^i)\mathcal{P}_j(\mathcal{F}^i)\mathcal{P}_j(m^i_{K\pi}) \quad (6)$$

for event i and category j.

In the event of significant signal in the inclusive $(K\pi)_0^{*0}$ or $K_2^*(1430)^0$ channels, we apply the *sPlot* technique [15] to the results of this first fit, which allows us to calculate a weight value for each event in each category (signal, $B\bar{B}$ background, etc.) based upon the covariance matrix from the likelihood fit and the value of the PDF for that event. Specifically, the *sWeight* for event i of category n is given by

$$w^i_n = \frac{\sum_{j=1}^{N_c} V_{nj}\mathcal{P}^i_j}{\sum_{k=1}^{N_c} Y_k \mathcal{P}^i_k}, \quad (7)$$

where N_c is the number of categories in the fit, V_{nj} is the covariance matrix element for categories n and j, and Y_k is the yield of category k.

The *sWeight* for a given event indicates how much that event contributes to the total yield in that category; *sWeights* can be less than zero or greater than one, but the sum of all *sWeights* for a given category reproduces the ML fit yield for that category.

The *sWeights* from this procedure are used to create two data sets: the *sWeighted* $(K\pi)_0^{*0}$ and $K_2^*(1430)^0$ signal samples. These weighted data sets allow us to determine the $\pi^+\pi^-$ mass distribution for the two signal samples of interest; these *sPlots* are faithful representations of $m_{\pi\pi}$ for the $(K\pi)_0^{*0}$ and $K_2^*(1430)^0$ signal components, assuming no correlation between $m_{\pi\pi}$ and the observables used to generate the *sWeights*. For signal MC, we find a maximum correlation of 8% between $m_{\pi\pi}$ and the other observables, with correlations typically less than 2%.

In the second stage, we fit the *sWeighted* $(K\pi)_0^{*0}$ and $K_2^*(1430)^0$ $m_{\pi\pi}$distributions to ρ^0 and f_0 hypotheses. A nonresonant $\pi^+\pi^-$ component is found to be consistent with zero. A $\sigma/f_0(600)$ component is considered in studies of systematic uncertainties (see Sec. XI). This fit gives us the final signal yield for the $\rho^0(K\pi)_0^{*0}$, $f_0(K\pi)_0^{*0}$, and $f_0K_2^*(1430)^0$ channels. This procedure also determines the $\rho^0K_2^*(1430)^0$ yield, but as we do not include helicity information in the fit, we cannot measure f_L, and thus we consider that channel a background.

Because of the two-stage nature of the $\rho^0/f_0(K\pi)_0^{*0}$ and $f_0K_2^*(1430)^0$ fits, the statistical uncertainty has two components. The first is from the uncertainty on the $m_{\pi\pi}$ fit to extract the fraction of ρ^0/f_0 events in the *sWeighted* sample. The second is a fraction of the uncertainty on the inclusive $(K\pi)_0^{*0}$ $(K_2^*(1430)^0)$ yield, the coefficient of which is given by the ratio of ρ^0 or f_0 events to the total number of inclusive $(K\pi)_0^{*0}$ $(K_2^*(1430)^0)$ signal events.

VII. SIGNAL AND BACKGROUND MODEL

PDF shapes for the signals and $B\bar{B}$ backgrounds are determined from fits to MC samples. For the $q\bar{q}$ category we use data sidebands, which we obtain by excluding the signal region. To parameterize the $q\overline{q}$ PDFs for all observables except $m_{\rm ES}$, we use the sideband defined by $m_{\rm ES} < 5.27$ GeV; to parameterize $m_{\rm ES}$, we require $|\Delta E| > 0.06$ GeV for ρ^0K^{*0} or $\Delta E < -0.12$ and $\Delta E > 0.08$ GeV for ρ^-K^{*+}. The excluded ΔE region is larger for ρ^-K^{*+} due to the poorer ΔE resolution resulting from having two π^0s in the final state.

Signal events selected from the MC contain both correctly and incorrectly reconstructed B meson candidates; the latter are labeled "self–cross feed" (SXF). SXF occurs either when some particles from the correct parent B meson are incorrectly assigned to intermediate resonances or when particles from the rest of the event are used in the signal B reconstruction. The fraction of SXF events ranges from 2–7% for $\rho^0/f_0 K^{*0}$ candidates and from 13–22% for $\rho^- K^{*+}$ candidates. We include both correctly reconstructed and SXF signal MC events in the samples used to parameterize the signal PDFs.

We use a combination of Gaussian, exponential, and polynomial functions to parameterize most of the PDFs. For the $m_{\rm ES}$ distribution of the $q\bar{q}$ background component, we use a parameterization motivated by phase-space arguments [16].

In the $K^*(892)$ (LMR) fits, the following observables are free to vary: the signal yields, longitudinal fraction f_L for $\rho K^*(892)$, and signal charge asymmetries $\mathcal{A}_{\rm ch}$; the $q\bar{q}$ background yields and background $\mathcal{A}_{\rm ch}$; and the parameters that most strongly influence the shape of the continuum background (the exponent of the phase-space–motivated $m_{\rm ES}$ function; dominant polynomial coefficients for ΔE, resonance masses, and helicities; fraction of real ρ, f_0, and K^* resonances in the background; and the mean, width, and asymmetry of the main Gaussian describing $\mathcal{F}$). For the HMR fits, the equivalent parameters are allowed to float, except no f_L or $\mathcal{A}_{\rm ch}$ parameters are included, and the $K^*(892)$ background yields are floated.

A. LASS parameterization of $(K\pi)^*_0$

The $J^P = 0^+$ component of the $K\pi$ spectrum, which we denote $(K\pi)^*_0$, is poorly understood; we generate MC using the LASS parameterization [4,5], which consists of the $K^*_0(1430)$ resonance together with an effective-range nonresonant component. The amplitude is given by

$$\mathcal{A}\,(m_{K\pi}) = \frac{m_{K\pi}}{q\cot\delta_B - iq} + e^{2i\delta_B}\frac{m_0\Gamma_0\frac{m_0}{q_0}}{(m_0^2 - m_{K\pi}^2) - im_0\Gamma_0\frac{q}{m_{K\pi}}\frac{m_0}{q_0}}, \quad (8)$$

$$\cot\delta_B = \frac{1}{aq} + \frac{1}{2}rq, \quad (9)$$

where $m_{K\pi}$ is the $K\pi$ invariant mass, q is the momentum of the $K\pi$ system, and $q_0 = q(m_0)$. We use the following values for the scattering length and effective-range parameters: $a = 2.07 \pm 0.10(\text{GeV})^{-1}$ and $r = 3.32 \pm 0.34(\text{GeV})^{-1}$ [5]. For the resonance mass and width we use $m_0 = 1.412$ GeV and $\Gamma_0 = 0.294$ GeV.

In the HMR, we parameterize the $m_{K\pi}$ distribution of the $(K\pi)^*_0$ signal category with a Gaussian convolved with an exponential. This shape reasonably approximates the LASS distribution, given the limited statistics in this analysis, and is chosen to reduce computation time. In the LMR, we use a linear polynomial, as only the tail of the $(K\pi)^*_0$ enters the LMR $m_{K\pi}$ region.

B. PDF corrections from data calibration samples

The decays $B^0 \to D^-\pi^+$ ($D^- \to K^+\pi^-\pi^-$) and $B^0 \to \bar{D}^0\pi^0$ ($\bar{D}^0 \to K^+\pi^-\pi^0$) have the same particle content in the final state as the signal, as well as large branching fractions. They are used as calibration channels. We apply the same selection criteria described in Secs. III, IV, and V, except that the $m_{\pi\pi}$ and $m_{K\pi}$ mass restrictions are replaced with $1.85 < m_{D^-} < 1.89$ GeV or $1.83 < m_{\bar{D}^0} < 1.89$ GeV and no D meson veto is applied. We use the selected data to verify that the ML fit performs correctly and that the MC properly simulates the $\mathcal{F}$, ΔE, and $m_{\rm ES}$ distributions. From these studies, we extract small corrections to the MC distributions of ΔE and $m_{\rm ES}$, which we apply to the signal PDFs in our LMR and HMR likelihood fits. We find that it is not necessary to correct the PDF for $\mathcal{F}$.

VIII. BACKGROUND $B^0 \to f_2(1270)K^*(892)^0$ YIELD FROM HIGH $m_{\pi^+\pi^-}$ SIDEBAND

To extract the $f_2(1270)K^*(892)^0$ yield, we select the LMR for $m_{K\pi}$ and require a $\pi^+\pi^-$ invariant mass within the range $0.47 < m_{\pi^+\pi^-} < 1.47$ GeV. We perform an ML fit with the observables ΔE, $m_{\rm ES}$, $\mathcal{F}$, and $m_{K\pi}$, and create a data set of *sWeighted* $K^*(892)^0$ events. We then fit the $m_{\pi^+\pi^-}$ spectrum of the *sWeighted* $K^*(892)^0$ events to ρ^0, f_0, and $f_2(1270)$ hypotheses (see Fig. 3). We find $627 \pm 41 f_2(1270)K^*(892)^0$ events after subtracting a 25 ± 13 event fit bias, which includes systematics; see Sec. IX for details of the fit bias estimation method. The MC efficiency ϵ of $B^0 \to f_2(1270)K^*(892)^0$ is 11.8% (longitudinal polarization) and 20.4% (transverse polarization).

Note that the three-component fit in Fig. 3 well describes the resonances of interest, though the fit quality is poor at

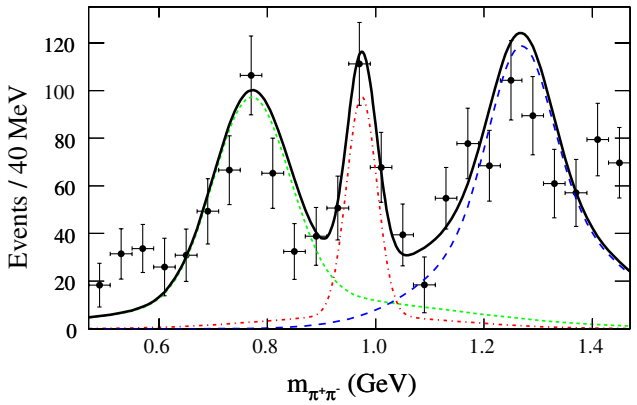

FIG. 3 (color online). (color online) $\pi^+\pi^-$ mass spectrum for *sWeighted* $K^*(892)^0$ events. The solid curve is the fit function, the [green] dotted curve is ρ^0, [red] dash-dotted curve is f_0, and [blue] dashed curve is $f_2(1270)$.

the lowest and highest $\pi^+\pi^-$ masses. As this study is intended to estimate the effect of higher resonances feeding into the nominal fit region, we determine that the three-component fit is sufficient. The excess of events in the low mass region could suggest the presence of a $\sigma/f_0(600)$ resonance; this is accounted for in a separate systematic study for the nominal fit. The excess in the highest bins could be explained by contributions from additional higher-mass resonances. As such resonances are unlikely to affect the ρ^0 and f_0 yields, we leave further understanding of these resonances for future studies.

Using the MC efficiency for $f_2(1270)K^*(892)^0$ in the LMR region, which includes a tighter cut on $m_{\pi\pi}$, and assuming $f_L = 0.5$, we determine that there are 47 ± 3 $f_2(1270)K^*(892)^0$ events expected in the LMR $\rho^0/f_0K^*(892)^0$ fit, as indicated in Table I.

IX. FIT VALIDATION

Before applying the fitting procedure to the data, we subject it to several tests. Internal consistency is verified by performing fits to ensembles of simulated experiments. From these, we establish the number of parameters associated with the $q\bar{q}$ PDF shapes that can be left free to float. Ensemble distributions of the fitted parameters verify that the generated values are reproduced with the expected resolution.

We investigate possible biases on the fitted signal yield Y_0, as well as on f_L for the $\rho K^*(892)$ channels, due to neglecting correlations among discriminating variables in the PDFs, as well as from cross feed from the $B\bar{B}$ background modes. To determine these biases, we fit ensembles of experiments into which we embed the expected number of signal and $B\bar{B}$ background events randomly extracted from detailed MC samples in which correlations are fully modeled. As correlations among fit variables are negligible for $q\bar{q}$ events, these events are generated from the PDFs. Each such experiment has the same number of signal and background candidates as the data. The measured biases are given in Table III. In calculating the branching fractions, we subtract the bias and include a systematic uncertainty (see Sec. XI) associated with the procedure.

The two-stage fit employed to determine the $\rho^0/f_0(K\pi)_0^{*0}$ and $f_0K_2^*(1430)^0$ yields (see Sec. VI B) complicates the validation procedure. We perform the first stage of the fit (which extracts the inclusive $(K\pi)_0^{*0}$ and $K_2^*(1430)^0$ yields) on ensembles of experiments, as described above. The bias obtained from this study is split between the ρ^0 and f_0 channels based on the relative fraction of ρ^0 or f_0 events to the total number of signal events in that sample.

X. FIT RESULTS

The branching fraction for each decay chain is obtained from

$$\mathcal{B} = \frac{Y - Y_0}{\epsilon N_B \prod \mathcal{B}_i}, \tag{10}$$

where Y is the yield of signal events from the fit, Y_0 is the fit bias discussed in Sec. IX, ϵ is the MC efficiency, $\mathcal{B}_i$ is the branching fraction for the ith unstable B daughter ($\mathcal{B}_i$ having been set to unity in the MC simulation), and N_B is the number of produced B^0 mesons. The values of $\mathcal{B}_i$ are taken from Particle Data Group world averages [2]. We assume the branching fractions of $\Upsilon(4S)$ to B^+B^- and $B^0\bar{B}^0$ to be the same and that each equals 50%. As the branching fractions $\mathcal{B}(f_0 \to \pi\pi)$ and $\mathcal{B}((K\pi)_0^* \to K\pi)$ are poorly known, we measure the products

$$\mathcal{B}(B^0 \to f_0K^*) \times \mathcal{B}(f_0 \to \pi\pi) \quad \text{and}$$
$$\mathcal{B}(B^0 \to X(K\pi)_0^*) \times \mathcal{B}((K\pi)_0^* \to K\pi).$$

We include the isospin ratios

TABLE III. Signal yield Y and its statistical uncertainty (see Sec. VI B for an explanation of the two errors on the $(K\pi)_0^{*0}$ and $K_2^*(1430)^0$ yields); fit bias Y_0; detection efficiency ϵ for longitudinal (ln) and transverse (tr) polarizations, if appropriate; daughter branching fraction product $\prod \mathcal{B}_i$; significance S including systematic uncertainties; measured branching fraction $\mathcal{B}$ with statistical and systematic errors; 90% C.L. upper limit (U.L.); longitudinal fraction f_L; and charge asymmetry $\mathcal{A}_{\rm ch}$. In the case of f_0K^{*0}, the quoted branching fraction is the product of $\mathcal{B}(B^0 \to f_0K^{*0}) \times \mathcal{B}(f_0 \to \pi\pi)$. For the $B^0 \to X(K\pi)_0^*$ channels, the quoted branching fraction is the product of $\mathcal{B}(B^0 \to X(K\pi)_0^*) \times \mathcal{B}((K\pi)_0^* \to K\pi)$. We include the isospin ratios $((K\pi)_0^{*0} \to K^+\pi^-) = 2/3$, $((K\pi)_0^{*+} \to K^+\pi^0) = 1/3$, and $(f_0 \to \pi^+\pi^-) = 2/3$.

Mode	Y (events)	Y_0 (events)	ϵ(ln) (%)	ϵ(tr) (%)	$\prod \mathcal{B}_i$ (%)	S (σ)	$\mathcal{B}$ (10^{-6})	U.L. (10^{-6})	f_L	$\mathcal{A}_{\rm ch}$
$\rho^0K^*(892)^0$	376 ± 37	44 ± 3	14.3	25.1	66.7	6.0	$5.1 \pm 0.6^{+0.6}_{-0.8}$	$\cdots$	$0.40 \pm 0.08 \pm 0.11$	$-0.06 \pm 0.09 \pm 0.02$
$\rho^0(K\pi)_0^{*0}$	$1045 \pm 36 \pm 118$	80 ± 11	9.6		66.7	6.3	$31 \pm 4 \pm 3$	$\cdots$	$\cdots$	$\cdots$
$f_0K^*(892)^0$	220 ± 23	2.1 ± 1.6	18.3		44.4	9.8	$5.7 \pm 0.6 \pm 0.4$	$\cdots$	$\cdots$	$+0.07 \pm 0.10 \pm 0.02$
$f_0(K\pi)_0^{*0}$	$88 \pm 19 \pm 10$	7 ± 1	12.5		44.4	3.0	$3.1 \pm 0.8 \pm 0.7$	$\cdots$	$\cdots$	$\cdots$
$f_0K_2^*(1430)^0$	$134 \pm 14 \pm 23$	0 ± 2	15.3		21.7	4.3	$8.6 \pm 1.7 \pm 1.0$	$\cdots$	$\cdots$	$\cdots$
$\rho^-K^*(892)^+$	167 ± 27	23 ± 3	4.9	11.2	33.3	5.1	$10.3 \pm 2.3 \pm 1.3$	$\cdots$	$0.38 \pm 0.13 \pm 0.03$	$+0.21 \pm 0.15 \pm 0.02$
$\rho^-(K\pi)_0^{*+}$	221 ± 74	-5 ± 8	4.5		33.3	2.8	$32 \pm 10 \pm 6$	<48	$\cdots$	$\cdots$

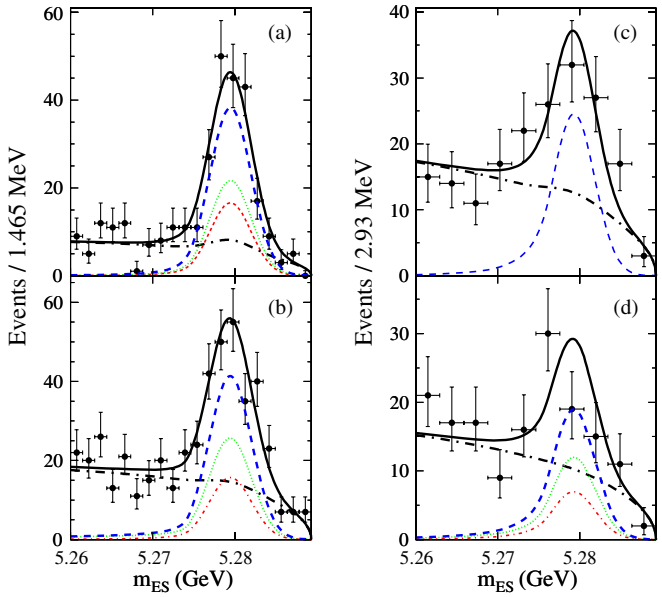

FIG. 4 (color online). (color online) B candidate $m_{\rm ES}$ projections for (a) $\rho^0/f_0 K^*(892)^0$ (b) inclusive $(K\pi)_0^{*0}$ and $K_2^*(1430)^0$, (c) $\rho^- K^*(892)^+$, (d) $\rho^-(K\pi)_0^{*+}$ and $\rho^- K_2^*(1430)^+$. The solid curve is the fit function, [black] long-dash–dotted curve is the total background, and the [blue] dashed curve is the total signal contribution. In (a), we separate the [red] dashed ρ^0 component from the [green] dotted f_0. In (b) and (d), $(K\pi)_0^*$ signal is [green] dotted and $K_2^*(1430)$ is [red] dashed. In (b), the two-stage nature of the fit means that the $(K\pi)_0^{*0}$ and $K_2^*(1430)^0$ signals include both f_0 and ρ^0 components, as the first stage of the HMR fit does not include information about the $\pi^+\pi^-$ mass spectrum.

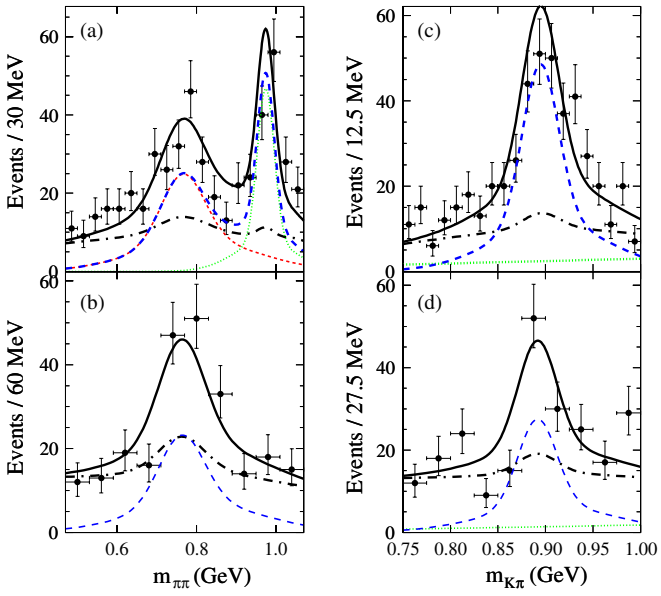

FIG. 5 (color online). (color online) Invariant mass projections for LMR (a, c) $\rho^0/f_0 K^*(892)^0$ and (b, d) $\rho^- K^*(892)^+$; $\pi\pi$ mass (left) and $K\pi$ mass (right). The solid curve is the fit function, [black] long-dash–dotted curve is the total background, and the [blue] dashed curve is the total signal contribution. In (a), we separate the [red] dashed ρ^0 component from the [green] dotted f_0. In (c) and (d), $(K\pi)_0^*$ background is [green] dotted.

$$\frac{\Gamma((K\pi)_0^{*0} \to K^+\pi^-)}{\Gamma((K\pi)_0^{*0} \to K\pi)} = \frac{2}{3},$$
$$\frac{\Gamma((K\pi)_0^{*+} \to K^+\pi^0)}{\Gamma((K\pi)_0^{*+} \to K\pi)} = \frac{1}{3},$$
$$\frac{\Gamma(f_0(980) \to \pi^+\pi^-)}{\Gamma(f_0(980) \to \pi\pi)} = \frac{2}{3}$$

in our calculations of $\prod \mathcal{B}_i$. The efficiency ϵ is evaluated from the simulation. For the $\rho^- K^{*+}$ channels, we apply an efficiency correction to the MC of roughly $97\%/\pi^0$. The specific values are determined by calculating a correction as a function of the π^0 lab momentum from a detailed MC simulation of the signal channel. The correction is determined from a study of tau decays to modes with π^0s as well as a study of $e^+e^- \to \gamma\omega$ with $\omega \to \pi^+\pi^-\pi^0$. The results for all signal channels are collected in Table III.

For all signals obtained from a one-stage ML fit, we determine the significance of observation S by taking the difference between the value of $-2\ln\mathcal{L}$ for the zero signal hypothesis and the value at its minimum. For the $\rho^0(K\pi)_0^{*0}$, $f_0(K\pi)_0^{*0}$, and $f_0 K_2^*(1430)^0$ channels, the fit method does not readily provide a $-2\ln\mathcal{L}$ distribution, so we determine the significance assuming Gaussian uncertainties, which provides a conservative lower limit on S.

For the $\rho^-(K\pi)_0^{*+}$ channel, which has a significance less than 3σ including systematics, we quote a 90% C.L. upper limit, given by the solution $\mathcal{B}_{90}$ to the equation

$$\frac{\int_0^{\mathcal{B}_{90}} \mathcal{L}(b)db}{\int_0^{\infty} \mathcal{L}(b)db} = 0.9, \qquad (11)$$

where $\mathcal{L}(b)$ is the value of the likelihood for branching fraction b. Systematic uncertainties are taken into account by convolving the likelihood with a Gaussian function representing the systematic uncertainties.

We show in Fig. 4 the data and fit functions projected onto the variable $m_{\rm ES}$, while in Fig. 5 we do the same for the $\pi\pi$ and $K\pi$ invariant masses for the LMR measurements. In Fig. 6(a) we project the data and fit functions from the first stage of the HMR $(K\pi)_0^{*0}$ and $K_2^*(1430)^0$ fits onto $m_{K^+\pi^-}$. In Figs. 4, 5, and 6(a) the signals are enhanced by the imposition of restrictions on the likelihood ratio, which greatly reduce the amount of background while retaining events that have a large probability to be signal.

Figs. 6(b) and 6(c) show the results of the second-stage HMR fit, distinguishing between the ρ^0 and f_0 hypotheses. In these plots, we do not impose a restriction on the likelihood ratio, as these *sWeighted* samples already contain only (b) $(K\pi)_0^{*0}$ or (c) $K_2^*(1430)^0$ signal events.

Ref. [5] extracts the resonant $K_0^*(1430)^0$ fraction of the LASS-parameterized $(K\pi)_0^{*0}$ distribution. The resonant

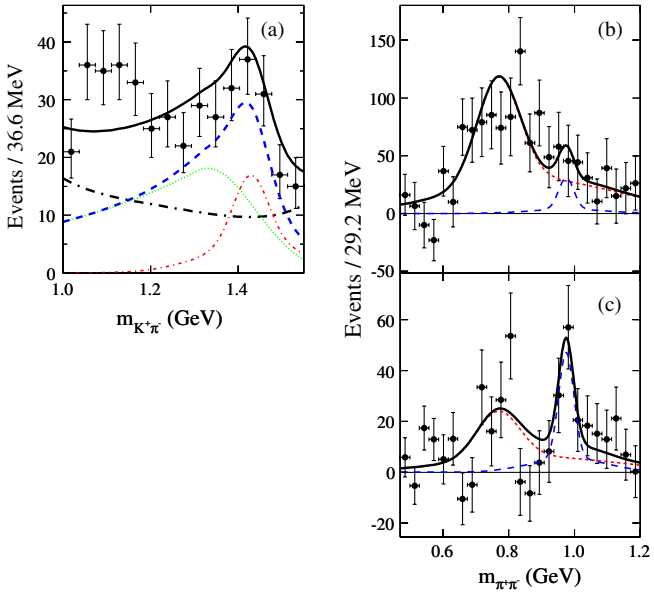

FIG. 6 (color online). (color online) Invariant mass projections for HMR $\rho^0(K\pi)_0^{*0}$, $f_0(K\pi)_0^{*0}$, and $f_0K_2^*(1430)^0$ signals (a) $K^+\pi^-$ mass, (b) $\pi^+\pi^-$ mass for *sWeighted* $(K\pi)_0^{*0}$ events, (c) $\pi^+\pi^-$ mass for *sWeighted* $K_2^*(1430)^0$ events. The solid curve is the fit function. In (a), the [black] long-dash–dotted curve is the total background, the [blue] dashed curve is the total signal contribution, the [green] dotted curve is the $(K\pi)_0^{*0}$ component, and the [red] dashed curve is $K_2^*(1430)^0$. In (b) and (c), the ρ^0 component is the [red] dashed curve and f_0 is the [blue] long-dashed curve.

fraction is found to account for 81% of the LASS shape in $B^+ \to (K\pi)_0^{*0}\pi^+$ decays. Using this resonant fraction along with the daughter branching fraction $\mathcal{B}(K_0^*(1430) \to K\pi) = (93 \pm 10)\%$ [2], we find the resonant branching fractions

$$\mathcal{B}(B^0 \to \rho^0 K_0^*(1430)^0) = (27 \pm 4 \pm 2 \pm 3) \times 10^{-6};$$
$$\mathcal{B}(B^0 \to f_0 K_0^*(1430)^0) \times \mathcal{B}(f_0 \to \pi\pi) = (2.7 \pm 0.7 \pm 0.5 \pm 0.3) \times 10^{-6};$$
$$\mathcal{B}(B^0 \to \rho^- K_0^*(1430)^+) = (28 \pm 10 \pm 5 \pm 3) \times 10^{-6},$$

where the uncertainties are statistical, systematic, and from the $K_0^*(1430) \to K\pi$ branching fraction, respectively.

XI. SYSTEMATIC UNCERTAINTIES

Table IV summarizes our estimates of the various sources of systematic uncertainty. We distinguish between uncertainties that concern a bias on the yield (additive) and those that affect the efficiency and total number of $B\bar{B}$ events (multiplicative), since only the former affect the significance of the results. The additive systematic uncertainties are the dominant source of systematics for the results presented in this paper. The final row of the table provides the total systematic error in units of branching fraction for each channel.

TABLE IV. Estimates of systematic uncertainties.

Quantity	ρ^0K^{*0}	$\rho^0K_0^{*0}$	f_0K^{*0}	$f_0K_0^{*0}$	$f_0K_2^{*0}$	ρ^-K^{*+}	$\rho^-K_0^{*+}$
Additive errors (events)							
ML fit	2.7	3.7	1.1	0.3	0.7	6.7	21.3
Fit bias	22.2	41.8	1.9	12.5	5.0	11.9	8.4
$B\bar{B}$ background	14.8	5.1	2.7	0.4	0.6	6.0	3.2
$f_0(980)$ parameters	3.5	10.0	8.8	10.0	2.5	...	...
LASS parameters	...	29.5	...	2.5	7.7	...	31.0
Interference	12.2	57.5	12.9	6.5	9.9	8.4	18.1
$\sigma/f_0(600)$	$^{+0.0}_{-36.0}$	$^{+0.0}_{-28.0}$	1.0	2.1	6.4	...	...
Total additive (events)	$^{+29.7}_{-46.6}$	$^{+77.9}_{-82.7}$	16.0	17.6	15.2	17.1	42.7
Total additive $[\mathcal{B}(10^{-6})]$	$^{+0.45}_{-0.71}$	$^{+2.58}_{-2.74}$	0.42	0.67	1.00	1.24	6.00
Multiplicative errors (%)							
Track multiplicity	1.0	1.0	1.0	1.0	1.0	1.0	1.0
Track finding	0.7	0.7	0.7	0.7	0.7	0.4	0.4
π^0 efficiency	...	...	...	...	...	3.8	3.6
Number $B\bar{B}$	0.6	0.6	0.6	0.6	0.6	0.6	0.6
Branching fractions	...	...	...	...	1.2	...	...
MC statistics	0.08	0.07	0.06	0.04	0.05	0.06	0.05
$\cos\theta_T$	1.5	1.5	1.5	1.5	1.5	1.5	1.5
PID	1.0	1.0	1.0	1.0	1.0	1.0	1.0
f_L uncertainty	5.8	...	...	...	...	2.1	...
Total multiplicative (%)	6.2	2.3	2.3	2.3	2.6	4.9	4.2
Total systematic $[\mathcal{B}(10^{-6})]$	$^{+0.6}_{-0.8}$	$^{+2.7}_{-2.8}$	0.4	0.7	1.0	1.3	6.1

A. Additive systematic errors

ML fit–We evaluate the systematic uncertainties due to the modeling of the signal PDFs by varying the relevant PDF parameters by uncertainties derived from the data control samples (see Sec. VII B). This uncertainty is larger for the $\rho^- K^{*+}$ channels, as the $\bar{D}^0\pi^0$ control sample has lower statistics than the $D^-\pi^+$ sample used for the $\rho^0 K^{*0}$ channels.

Fit bias–The fit bias arises mostly from correlations among the fit variables, which are neglected in the ML fit. Studies of this bias are described in Sec. IX. The associated uncertainty is the sum in quadrature of half the correction and its statistical uncertainty. For the $\rho^0/f_0(K\pi)_0^{*0}$ and $f_0 K_2^*(1430)^0$ channels, we add the uncertainty on the total bias in quadrature with half the bias scaled by the ratio of ρ^0 or f_0 events to their sum.

$B\bar{B}$ background–We estimate the uncertainty from the fixed $B\bar{B}$ background component yields by repeating the fit with the yields of these components varied by their uncertainties. For each signal channel, we add in quadrature the change in signal yield from varying each $B\bar{B}$ background, and quote this as the systematic. The uncertainty on the measured $\rho(K\pi)_0^*$ branching fractions makes this a large systematic for $\rho^0 K^*(892)^0$ and $\rho^- K^*(892)^+$.

$f_0(980)$ parameters–The width of the f_0 is not accurately measured; to account for this, we allow the mean and width of the f_0 to float in the LMR fit and take half the shift in the signal yield as a systematic. This is one of the largest systematics for $f_0 K^*(892)^0$. In the HMR, we lack the statistics to allow these parameters to float, and so we perform the fit with them fixed to the parameters obtained when floating them in the LMR. This is among the largest systematics for $f_0(K\pi)_0^{*0}$ and $\rho^0(K\pi)_0^{*0}$.

LASS shape parameters–For the $(K\pi)_0^*$ channels, we vary the LASS parameters in the MC by the uncertainties listed in Sec. VII A and refit the data sample with PDF parameters based on this new MC. In each channel, we take the largest variation in the yield as a result of this procedure as the systematic. The LASS systematic is the dominant one for $\rho^-(K\pi)_0^{*+}$.

ρ^0/f_0 interference–The interference between the ρ^0 and f_0 integrates to zero over the symmetric $\mathcal{H}_\rho$ range. Additionally, the differential rate is an odd function of $\mathcal{H}_\rho$, so the fact that we use $|\mathcal{H}_\rho|$ in the fit means that the interference term also vanishes from the differential rate.

K^* interference–In our nominal fits, we do not account for interference between the scalar and vector K^*, or between the vector and tensor. We estimate the magnitude of the K^* interference effect in a separate calculation, which takes into account the relevant mass and helicity acceptance functions and varies the relative strong phases between components over the full range. As interference can affect the K^* line shape, we conservatively take this systematic to be additive. This is among the dominant systematic uncertainties in the HMR fits.

$f_2(1270)$ interference–The fit described in Sec. VIII, used to estimate the background from $B^0 \to f_2(1270)K^*(892)^0$ decays, is performed without interference. Interference terms vanish when integrating over the full solid angle; however, the requirement that the helicity angle be $|\mathcal{H}_\rho| < 0.9$ leaves a nonzero interference term. For the case of interference between the f_0 and $f_2(1270)$, the scalar f_0 may interfere with the longitudinal component of the $f_2(1270)$. Adding this term to the fit results shown in Fig. 3, assuming $f_L = 0.5$ for the $f_2(1270)$, and scanning over the unknown phase difference between the f_0 and $f_2(1270)$, we find a maximum yield difference between the case of no interference of $\pm 8.4\%$ in the f_0 region. As the interference depends upon the sine of the unknown phase, we divide by $\sqrt{2}$ and report an additive $f_0 - f_2(1270)$ interference systematic of 12.8 events (5.8%). Using a similar procedure for $\rho^0 - f_2(1270)$ interference, we report a systematic of 6.8 events (1.8%). For the $f_0 K^*(892)^0$ measurement, this is the dominant systematic.

$\sigma/f_0(600)$ resonance–The scalar $\sigma/f_0(600)$ is poorly understood and its parameters uncertain. We estimate the effect of a possible $\sigma/f_0(600)$ resonance by including $\sigma/f_0(600)K^*$ as a separate component in our fits. We parameterize the $\sigma/f_0(600)$ using a relativistic Breit-Wigner function with $m = 513$ MeV and $\Gamma = 335$ MeV [17]. As we lack $\sigma/f_0(600)K^*$ MC, for the LMR $K^*(892)^0$ fit we use the $f_0 K^{*0}$ PDF shapes for all variables except the $\pi^+\pi^-$ invariant mass. We use the average $\sigma/f_0(600)K^{*0}$ branching fraction from the three K^{*0} channels to calculate how many $\sigma/f_0(600)K^{*0}$ events are expected in each K^{*0} sample; this $\sigma/f_0(600)K^{*0}$ yield is then fixed in each fit. We take 100% of the resulting signal yield variation as a low-side systematic for the ρ^0 channels (a nonzero $\sigma/f_0(600)$ yield decreases the ρ^0 yield) and conservatively consider this a two-sided systematic in the f_0 channels. This is the dominant systematic for $\rho^0 K^*(892)^0$.

B. Multiplicative systematic errors

Track multiplicity–The inefficiency of the selection requirements for the number of tracks in the event is a few percent. We estimate an uncertainty of 1% from the uncertainty in the low-multiplicity tail of the B decay model.

Track finding/efficiency–Studies of tau events determine that no efficiency correction is necessary for track finding and reconstruction. The systematic uncertainty is determined by adding linearly 0.17% per track in quadrature with an overall factor of 0.11%.

π^0 reconstruction efficiency–We apply an efficiency correction to the MC of roughly $97\%/\pi^0$; the correction depends on the π^0 momentum spectrum, so it is somewhat different in different channels. The uncertainty associated with this correction is roughly $1.5\%/\pi^0$.

Number of $B\bar{B}$ events–A separate study [18] determines the overall uncertainty on the number of produced $B\bar{B}$ pairs to be 0.6%.

TABLE V. Estimates of systematic errors on f_L.

Quantity	$\rho^0 K^*(892)^0$	$\rho^- K^*(892)^+$
ML fit	0.003	0.012
Fit bias	0.046	0.016
$B\bar{B}$ background	0.019	0.024
$f_0(980)$ parameters	0.004	···
$\sigma/f_0(600)$	0.100	···
Total	0.112	0.031

Branching fractions of decay chain daughters–This is taken as the uncertainty on the daughter particle branching fractions from Ref. [2].

MC statistics–The uncertainty due to finite signal MC sample sizes (typically 430,000 generated events) is given in Table IV.

Event shape requirements–Uncertainties due to the $\cos\theta_T$ requirement are estimated from data control samples to be $0.05 \times (1 - (|\cos\theta_T|\text{cut value}))$.

PID–We estimate from independent samples that the average efficiency uncertainty associated with particle identification is 1.0%.

f_L *uncertainty*–The signal yield reconstruction efficiency for VV channels depends on f_L. As a result, any systematic uncertainty on f_L translates into a systematic uncertainty on the efficiency through the following expression:

$$\frac{\Delta\epsilon}{\epsilon} = \frac{\epsilon_L - \epsilon_T}{f_L\epsilon_L + (1 - f_L)\epsilon_T}\Delta f_L. \tag{12}$$

The systematic error on f_L (Δf_L)is given in Table V.

C. Charge asymmetry systematic errors

From the analysis of a variety of data control samples, the bias on $\mathcal{A}_{\rm ch}$ is found to be negligible for pions and -0.01 for kaons, due to differences between K^+ and K^- interactions in the detector material. We correct the fitted $\mathcal{A}_{\rm ch}$ by $+0.01$ and assign a systematic uncertainty of 0.02, mainly due to the bias correction.

D. Systematic errors on f_L

Most systematic uncertainties cancel when calculating f_L. We include uncertainties from the signal PDF modeling (''ML fit''), fit bias (for which we assign an uncertainty equal to 100% of the bias added in quadrature with its uncertainty), $B\bar{B}$ background yields, the f_0 parameterization, and the possible existence of a $\sigma/f_0(600)$ (where we take 100% of the f_L variation when the $\sigma/f_0(600)K^{*0}$ is fixed in the study described in Sec. XI A). For $\rho^0 K^*(892)^0$, the fit bias of -0.045 ± 0.008 provides a moderate uncertainty; for $\rho^- K^*(892)^+$, this bias is small (-0.009 ± 0.014). See Table V for details.

XII. DISCUSSION AND SUMMARY OF RESULTS

We obtain the first observations of $B^0 \to \rho^0(K\pi)_0^{*0}$, $f_0 K^*(892)^0$, and $\rho^- K^*(892)^+$ with greater than 5σ significance, including systematics. We present the first evidence for $B^0 \to f_0(K\pi)_0^{*0}$ and $f_0 K_2^*(1430)^0$, which we observe with a significance of 3.0σ and 4.3σ, respectively. All branching fraction measurements have greater than 3σ significance including systematics, except $\rho^-(K\pi)_0^{*+}$, for which we also quote a 90% C.L. upper limit. No significant direct CP violation is observed. Our results are consistent with and supersede those reported in Ref. [6].

For the $K^*(892)$ channels, we find the following results:

$$\mathcal{B}(B^0 \to \rho^0 K^{*0}) = (5.1 \pm 0.6^{+0.6}_{-0.8}) \times 10^{-6};$$
$$f_L(\rho^0 K^{*0}) = 0.40 \pm 0.08 \pm 0.11;$$
$$\mathcal{A}_{\rm ch}(\rho^0 K^{*0}) = -0.06 \pm 0.09 \pm 0.02;$$
$$\mathcal{B}(B^0 \to \rho^- K^{*+}) = (10.3 \pm 2.3 \pm 1.3) \times 10^{-6};$$
$$f_L(\rho^- K^{*+}) = 0.38 \pm 0.13 \pm 0.03;$$
$$\mathcal{A}_{\rm ch}(\rho^- K^{*+}) = +0.21 \pm 0.15 \pm 0.02;$$
$$\mathcal{B}(B^0 \to f_0 K^{*0}) \times \mathcal{B}(f_0 \to \pi\pi) = (5.7 \pm 0.6 \pm 0.4) \times 10^{-6};$$
$$\mathcal{A}_{\rm ch}(f_0 K^{*0}) = +0.07 \pm 0.10 \pm 0.02.$$

The $\rho^0 K^*(892)^0$ results agree with previous *BABAR* [6] and Belle [7] measurements and are consistent with predictions from QCDF [9]. The $\rho^- K^*(892)^+$ results are consistent with the previous *BABAR* upper limit and agree with QCDF predictions. Both the $\rho^0 K^*(892)^0$ and $\rho^- K^*(892)^+$ branching fractions are, however, higher than the values predicted by QCDF. We find a branching fraction for $f_0 K^*(892)^0$ within the previous *BABAR* 90% C.L. upper limit (6.5×10^{-6})[6] and somewhat above the Belle limit (3.3×10^{-6})[7], where we have scaled the published limits by a factor of 3/2, as the previous analyses assumed $\mathcal{B}(f_0 \to \pi^+\pi^-) = 100\%$, whereas this measurement includes the isospin ratio $\Gamma(f_0 \to \pi^+\pi^-)/\Gamma(f_0 \to \pi\pi) = 2/3$. The $f_0 K^*(892)^0$ branching fraction result is within one sigma of the QCDF prediction of $4.8^{+5.3}_{-2.0} \times 10^{-6}$, which is scaled by a factor of 3/4, as Ref. [9] assumes $\mathcal{B}(f_0 \to \pi^+\pi^-) = 0.5$. We note that a previous *BABAR* study of $B \to \phi K^*$ [19] observed an excess of $B^0 \to (K^+K^-)_0 K^*(892)^0$ events, where the scalar $(K^+K^-)_0$ could include $f_0(980)$ decays. If we assume all the observed $(K^+K^-)_0$ excess to be from $f_0 \to K^+K^-$ and follow Ref. [2] in defining the ratio $R = \Gamma(\pi\pi)/[\Gamma(\pi\pi) + \Gamma(K\bar{K})] \sim 0.75$, then the $B^0 \to f_0 K^*(892)^0$ branching fractions are comparable for the $f_0 \to \pi^+\pi^-$ and K^+K^- channels.

As expected for penguin-dominated channels, the measured f_L values are inconsistent with the naïve

factorization prediction of $f_L \sim 1$. The predicted f_L for $\rho^- K^{*+}$ is higher than the measured value, though the theory errors are still large. Including the results from this paper and averaging *BABAR* [6] and Belle [7] f_L measurements for $\rho^+ K^{*0}$, we can order the experimentally measured values of f_L [6–8] as

$$f_L(\rho^- K^{*+}) \lesssim f_L(\rho^0 K^{*0}) \lesssim f_L(\rho^+ K^{*0}) < f_L(\rho^0 K^{*+}),$$

with the values ranging from 0.38–0.78. With the current experimental sensitivities, the three smallest f_L values are consistent with each other at 1σ. QCDF [9] predicts the following hierarchy among these f_L values

$$f_L(\rho^0 K^{*0}) < f_L(\rho^+ K^{*0}) < f_L(\rho^- K^{*+}) < f_L(\rho^0 K^{*+}),$$

which agrees with the experimental finding that $f_L(\rho^0 K^{*+})$ is largest. A more rigorous test of the theoretical hierarchy requires additional experimental input.

For $f_0(K\pi)_0^{*0}$ and $f_0 K_2^*(1430)^0$, we find

$$\begin{aligned}
&\mathcal{B}(B^0 \to f_0(K\pi)_0^{*0}) \times \mathcal{B}(f_0 \to \pi\pi) \times \mathcal{B}((K\pi)_0^* \to K\pi) \\
&\quad = (3.1 \pm 0.8 \pm 0.7) \times 10^{-6}; \\
&\mathcal{B}(B^0 \to f_0 K_2^*(1430)^0) \times \mathcal{B}(f_0 \to \pi\pi) \\
&\quad = (8.6 \pm 1.7 \pm 1.0) \times 10^{-6}.
\end{aligned}$$

For $\rho(K\pi)_0^*$, we find

$$\begin{aligned}
&\mathcal{B}(B^0 \to \rho^0(K\pi)_0^{*0}) \times \mathcal{B}((K\pi)_0^* \to K\pi) \\
&\quad = (31 \pm 4 \pm 3) \times 10^{-6}; \\
&\mathcal{B}(B^0 \to \rho^-(K\pi)_0^{*+}) \times \mathcal{B}((K\pi)_0^* \to K\pi) \\
&\quad = (32 \pm 10 \pm 6) \times 10^{-6}; \\
&\quad < 48 \times 10^{-6}.
\end{aligned}$$

Using the $K_0^*(1430)^0$ resonant fraction of the LASS $(K\pi)_0^{*0}$ result from Ref. [5], we can calculate the branching fractions for the $K_0^*(1430)$ component of our $(K\pi)_0^*$ channels. We find

$$\begin{aligned}
&\mathcal{B}(B^0 \to \rho^0 K_0^*(1430)^0) = (27 \pm 4 \pm 2 \pm 3) \times 10^{-6}; \\
&\mathcal{B}(B^0 \to f_0 K_0^*(1430)^0) \times \mathcal{B}(f_0 \to \pi\pi) \\
&\quad = (2.7 \pm 0.7 \pm 0.5 \pm 0.3) \times 10^{-6}; \\
&\mathcal{B}(B^0 \to \rho^- K_0^*(1430)^+) = (28 \pm 10 \pm 5 \pm 3) \times 10^{-6},
\end{aligned}$$

where the third uncertainty is from the daughter branching fraction $\mathcal{B}(K_0^*(1430) \to K\pi) = (93 \pm 10)\%$ [2]. These results are somewhat lower than the QCDF predictions [9] but are consistent with QCDF within the uncertainties. The pQCD predictions have central values of $(0.5\text{–}10) \times 10^{-6}$ and are, in most cases, inconsistent with our results.

ACKNOWLEDGMENTS

We are grateful for the extraordinary contributions of our PEP-II colleagues in achieving the excellent luminosity and machine conditions that have made this work possible. The success of this project also relies critically on the expertise and dedication of the computing organizations that support *BABAR*. The collaborating institutions wish to thank SLAC for its support and the kind hospitality extended to them. This work is supported by the U.S. Department of Energy and the National Science Foundation, the Natural Sciences and Engineering Research Council (Canada), the Commissariat à l'Energie Atomique and Institut National de Physique Nucléaire et de Physique des Particules (France), the Bundesministerium für Bildung und Forschung and Deutsche Forschungsgemeinschaft (Germany), the Istituto Nazionale di Fisica Nucleare (Italy), the Foundation for Fundamental Research on Matter (the Netherlands), the Research Council of Norway, the Ministry of Education and Science of the Russian Federation, Ministerio de Ciencia e Innovación (Spain), and the Science and Technology Facilities Council (United Kingdom). Individuals have received support from the Marie-Curie IEF program (European Union) and the A. P. Sloan Foundation (USA).

[1] H.-Y. Cheng and J. G. Smith, Annu. Rev. Nucl. Part. Sci. **59**, 215 (2009).
[2] K. Nakamura *et al.* (Particle Data Group), J. Phys. G **37**, 075021 (2010).
[3] The mass and width of the $f_0(980)$ are from the Breit-Wigner parameters obtained by the E791 Collaboration: E. M. Aitala *et al.* (E791 Collaboration), Phys. Rev. Lett. **86**, 765 (2001).
[4] D. Aston *et al.* (LASS Collaboration), Nucl. Phys. **B296**, 493 (1988).
[5] B. Aubert *et al.* (*BABAR* Collaboration), Phys. Rev. D **72**, 072003 (2005); **74**, 099903 (2006).
[6] B. Aubert *et al.* (*BABAR* Collaboration), Phys. Rev. Lett. **97**, 201801 (2006).
[7] S. H. Kyeong *et al.* (Belle Collaboration), Phys. Rev. D **80**, 051103 (2009); K. Abe *et al.* (Belle Collaboration), Phys. Rev. Lett. **95**, 141801 (2005).

[8] P. del Amo Sanchez *et al.* (*BABAR* Collaboration), Phys. Rev. D **83**, 051101 (2011).
[9] H. Y. Cheng and K. C. Yang, Phys. Rev. D **78**, 094001 (2008); **79**, 039903 (2009); M. Beneke, J. Rohrer, and D. Yang, Nucl. Phys. **B774**, 64 (2007); H. Y. Cheng, C. K. Chua, and K. C. Yang, Phys. Rev. D **77**, 014034 (2008).
[10] Z. Q. Zhang, Phys. Rev. D **82**, 034036 (2010).
[11] B. Aubert *et al.* (*BABAR* Collaboration), Nucl. Instrum. Methods Phys. Res., Sect. A **479**, 1 (2002).
[12] The *BABAR* detector Monte Carlo simulation is based on GEANT4, S. Agostinelli *et al.*, Nucl. Instrum. Methods Phys. Res., Sect. A **506**, 250 (2003).EVTGEN, D. J. Lange, Nucl. Instrum. Methods Phys. Res., Sect. A **462**, 152 (2001).
[13] S. Brandt Ch. Peyrou, R. Sosnowski, and A. Wroblewski, Phys. Lett. **12**, 57 (1964); E. Farhi, Phys. Rev. Lett. **39**, 1587 (1977).
[14] B. Aubert *et al.* (*BABAR* Collaboration), Phys. Rev. D **79**, 072009 (2009).
[15] M. Pivk and F. R. Le Diberder, Nucl. Instrum. Methods Phys. Res., Sect. A **555**, 356 (2005).
[16] H. Albrecht *et al.* (ARGUS Collaboration), Phys. Lett. B **241**, 278 (1990).
[17] H. Muramatsu *et al.* (CLEO Collaboration), Phys. Rev. Lett. **89**, 251802 (2002); **90**, 059901 (2003).
[18] G. D. McGregor, arXiv:0812.1954.
[19] B. Aubert *et al.* (*BABAR* Collaboration), Phys. Rev. D **78**, 092008 (2008).